Kinetics of CO methanation using a Fe-bearing catalyst from a blast furnace sludge.

Paulina Melo Bravo[a,1], Romel Jiménez[a], François Devred[c], Damien P. Debecker[c] , Claudia Ulloa[b], Ximena García[a*]

[a] Carbon and Catalysis Laboratory (CarboCat), Department of Chemical Engineering, Faculty of Engineering, Universidad de Concepción, P.O Box 160-C, Concepción, Chile.

[b] Environmental Engineering Department, Faculty of Environmental Sciences and EULA Chile Centre, Universidad de Concepción, P.O Box 160-C, Concepción, Chile.

[c]. Institute of Condensed Matter and Nanoscience (IMCN), UCLouvain, Place Louis Pasteur 1, 1348 Louvain-La-Neuve, Belgium

* Corresponding author: xgarcia@udec.cl

ABSTRACT

Hydrogenation of CO for methane production was studied using blast furnace sludge (BFS), a Fe-rich residue, as a catalyst. Previously, the raw BFS was subjected to successive leaching stages to reduce some inhibitor compounds. The catalytic runs were carried out in a laboratory scale differential reactor, at 300-350°C, 1 atm, and variable partial pressures of H_2 (10 – 50 kPa) and CO (0.25 - 3.0 kPa). Before the reaction, the catalyst was reduced in H_2 at 500°C for 2 hours. Product gases were analyzed by gas chromatography. The BFS, leached (BFS-L) and reduced (BFS-L-R) catalysts were characterized by atomic absorption spectroscopy (AAS), in situ X-ray diffraction (XRD), N_2-physisorption at 77K and thermogravimetric-mass spectrometry analysis (TG-MS). Some selected samples were also analyzed by X-ray photoelectron spectroscopy (XPS). Iron content in the leached

[1] Present address: Institute of Condensed Matter and Nanoscience (IMCN), UCLouvain, Place Louis Pasteur 1, 1348 Louvain-La-Neuve, Belgium.

sample was 51.7 wt%, present mostly as hematite (Fe_2O_3) and magnetite (Fe_3O_4). Carbon was also detected in the BFS-L, although its influence on CH_4 formation was found to be negligible. When BFS-L was used as a catalyst, at 320°C and H_2/CO=20:1, rate of methane production and selectivity achieved 2.63 μmolCH_4/g_{cat}·min and 49.5% respectively. Experimental results demonstrated that, under the studied conditions, CO hydrogenation towards CH_4 proceeds through an H_2-assisted reaction path. Langmuir-Hinshelwood rate laws for both CH_4 and the undesired CO_2 production were derived, and parameters were adjusted from the obtained data. The activation energy for methane formation was 93.2 kJ/mol.

To evaluate the catalyst resistance to poisoning, a BFS-L sample was treated with SO_2 prior to the reaction tests. A first-order deactivation model was consistent with the data. The results of this work demonstrate the feasibility of BFS as a low-cost precursor of a methanation catalyst. Although this is a realistic alternative, further research, both experimental and modeling is still required to optimize operating conditions and to explore different reactor configurations.

Keywords: Blast furnace sludge, CO methanation, Fe-based catalyst, kinetics, deactivation

1. Introduction

Natural gas is a highly efficient form of energy and is considered to be one of the cleanest fossil fuel [1]. Burning natural gas could help to improve air quality since natural gas produce negligible amounts of SO_2, mercury, particulate matter, NOx and emits less CO_2 compared to other fossil fuels [2]. In a recent publication [3], emission factors for different fuels were evaluated and compared, using the same methodology. Results showed that for coal, the carbon dioxide emission factor relative to net calorific value is the highest (1396 g CO_2/kWh), whereas shale gas had the lowest value (205 g CO_2/kWh). For natural gas, a mean value of 210 g CO_2/kWh was reported.

Due to rapid urbanization and industrial growth, natural gas consumption rose by an estimated 4.6% in 2018, its highest annual growth rate since 2010 [4]. The increasing demand and price volatility of this important energy source have increased the interest, in many regions of the world, to produce

synthetic natural gas (SNG) from different resources such as coal, biomass and organic solid wastes [5, 6]. In addition, SNG production constitutes an efficient and clean way for the exploitation of coal and biomass energy in those countries where natural gas is not available [7, 8].

In the SNG process, the so-called *methanation reaction*, in which methane is synthesized by CO hydrogenation with the aid of a catalyst, is a critical step [9-11]. The basic requirements for the ideal methanation catalyst include low cost, good low-temperature activity and high stability [12-13]. Although Ni-based catalysts are preferred in methanation reaction, some problems still exist, such as carbon deposition, sintering and sulfur poisoning [6, 14].

Other elements of group VIII, such as Ru and Rh have shown high activity and selectivity. However, their high cost has inhibited its use at larger scales [15]. Another element of this group is iron (Fe), which has shown promising behaviors in CO methanation showing the best activity/price ratio, both for methanation and Fischer-Tropsch synthesis (FTS) [16]. For the syngas methanation reaction, addition of Fe on monometallic Ni has been attempted to enhance catalytic activity and stability of Nickel [17-21]. Additionally, iron–based catalysts are used in Fisher Tropsch Syntheses (FTS) due to their higher resistance to sulfur poisoning and high activity [22]. Development of catalysts for direct conversion of CO-rich syngas to methane and lower olefins (C_2-C_4) is of increasing scientific and industrial interest [6, 23].

It has been demonstrated that the selectivity towards the production of CH_4 is favored at high H_2 pressures and low temperatures and it is inhibited by high partial pressures of CO [18, 24]. The secondary reactions that affect methane formation are the water gas shift ($CO + H_2O = CO_2 + H_2$) and the Boudouard ($2CO = C + CO_2$) reactions [25, 26]. Even though, the formation of paraffins, olefins, and alcohols should not be ruled out, their selectivity on Fe catalysts is generally favored at high pressures ($P \geq 20$bar), low H_2/CO ratios and low temperatures (200 – 260°C) [25, 27, 28].

Although several researchers have studied the kinetic modeling on Fe-based catalysts for FTS, there is no general agreement in the form of the reaction rate expression [29, 30]. Langmuir-Hinshelwood-Hougen-Watson (LHHW) mechanism represents the most applied model for industrial applications [31]. Reaction paths reported for FTS require the dissociation of adsorbed CO in two possible ways, i) without the assistance of hydrogen, to give carbide species on the C* surface, which correspond to

the intermediary specie for all reaction products [32, 33], or ii) assisted by hydrogen, with HCO* and HCOH* formation, ending in the CH* form as an intermediary compound [34, 35]. Some authors claim that, in Fe-catalyzed methanation, the dissociation mechanism assisted by H* predominates at high H_2 partial pressures (greater than 2 bar) [36, 37]. Others have reported that the dissociation of the C-O bond occurs mainly without the assistance of H* [24, 38, 39]. Lo et al. [25] used DFT (Density Functional Theory) calculations to propose that the dissociation of CO on the Fe surface occurs without the assistance of H* and that the formation of CH_4 is due to successive hydrogenations of adsorbed carbon. Ojeda et al. [36] demonstrated, experimentally and via DFT studies, that the mechanism of formation of hydrocarbons on Fe catalysts promoted with Zn, Cu, K, considers the H*-assisted dissociation of CO with subsequent addition of adsorbed Hydrogen to form CH* monomers and water, together with the formation of CO_2 by adding O* to a molecule of CO*. It has been reported that the chemisorbed species CO* and H* predominate on the surface of the Fe catalyst [37]. Discussions are still ongoing.

In a circular economy, transforming industrial wastes into useful materials has attracted increasing attention [40, 41]. One relevant example is the steel making industry, which generates important amounts of hazardous solid wastes as by-products (sludge and slags) that are generally discarded to the environment or disposed in specific landfills [42, 43]. Blast furnace sludge (BFS), a Fe- rich material, is one of the less recycled wastes [44]. Although the use of such wastes does not alleviate disposal problems, their valorization, in our case, as a Fe-bearing methanation catalyst precursor can provide an inexpensive and sustainable route to SNG production. Other challenges faced by the steel industry consist of the upgrading of different top gases produced during the process [45, 46]. The presence of important amounts of CO in coke oven and blast furnace gases makes them suitable for its methanation and subsequent use in the steel making process. One remarkable characteristic of this waste, reported in the literature [44, 47, 48] and verified through continuous tracking (carried out by the Steel Company) is its homogeneity, which show no important variations on its chemical composition along time.

In this work, BFS from the Chilean steel company, CAP steel-Huachipato, is activated and used as an active Fe-based catalyst for the H_2-enriched syngas methanation reaction. All samples are roughly

characterized, and catalytic activity is experimentally quantified by determining the effect of different reaction conditions (temperature, H_2/CO ratio) on i) the rate of methane formation, ii) the CH_4 selectivity, and iii) the stability against sulfur.

Some insights of the reaction mechanisms are proposed and from these, a Langmuir-Hinshelwood model is derived. This article can be regarded as a contribution to a more sustainable catalysis and provides relevant information for process design and scaling.

2. Experimental

2.1. Waste material (catalyst precursor)

A blast furnace sludge (BFS) is selected as the Fe-based catalyst precursor. This residue comes from the Huachipato plant of the Pacific Steel Company (CAP S.A.), located in the Bio Bio region in Chile. The BFS is generated from the wet off-gas cleaning process of the blast furnace and, besides iron and other inorganic elements, contains approximately 25% moisture.

2.2. BFS characterization

The BFS samples (fresh and pretreated) were characterized by different techniques. The determination of major inorganic elements was carried out by atomic absorption spectroscopy (AAS), using an Agilent 280FS AA spectrometer. X-ray diffraction (XRD) was selected to characterize the Fe- and other crystalline phases. A D4 ENDEAVOR diffractometer equipped with the D-Max/A system for the acquisition of diffraction patterns was used. This possesses a radiation source from anode CuKα with a λ of 0.15518 nm and Mn filters, and operates at 35 kV and 15 mA. Sweep speed was 1 º/min with a step of 0.020 ° in a range between 3 °< 2θ < 70 °. Additionally, in situ XRD was used to identify the Fe phases while subjecting the BFS sample to the reduction pre-treatment (10 ml/min of 10%H_2/He from room temperature to 800 ºC). A D8 Brunker diffractometer was used. These results were compared with a hematite standard sample under the same conditions.

BET surface area was determined by N_2 adsorption at 77 K in a Micromeritics Gemini VII 2390t. All samples were previously degassed at 300 °C during 4 h under N_2 atmosphere. X-ray photoelectron spectroscopy (XPS) was used to compare relative composition of surface elements, on the BFS,

BFS-L and on a hematite standard, particularly Fe, Ca, Zn, Si, Al, and C. The spectrometer corresponds to the model SSX 100/206 equipped with a monochromatized micro focus with AlKα X-ray source, which operates at 10 kV and 12 mA.

2.3. Catalyst preparation

2.3.1. Extractive leaching

In order to isolate the effect of Fe on catalytic activity and to prevent possible deactivation caused by the accompanying elements, BFS was subjected to two successive extractions steps using ammonium acetate 1.0 M (pH: 4.5) (Step 1), and hydroxylamine chlorhydrate 0.1 M in 0.01 M HNO_3 (pH: 2) (Step 2), to extract exchangeable elements Ca^{2+}, Mg^{2+} and K^{+}. The leached sample, denominated as BFS-L, was also characterized by elemental analysis (LECO TrueSpecCHN) and atomic absorption spectroscopy (Agilent 280FS AA).

2.3.2. Catalyst activation

Since the Fe particles must be in their reduced form (ideally as Fe^0) to be suitable for its use as a catalyst for CO methanation, an activation step, consisting in the reduction of the Fe phases, Fe_2O_3 and Fe_3O_4, under H_2 was carried out. The reduction steps are given by Eq. 1:

$$Fe_2O_3 \xrightarrow{H_2} Fe_3O_4 \xrightarrow{H_2} FeO \xrightarrow{H_2} Fe^0 \quad \text{(Eq.1)}$$

To determine the activation conditions, a reducibility test was conducted in a thermogravimetric system (TGA), Netzsch STA 409 Luxx, coupled to a mass spectrometer QMS 403 Aëolos. 20 mg of sample was heated from room temperature up to 800 °C, under 80 ml/min H_2 at a rate of 10 °C/min. From these results, the reduction conditions for catalyst activation were selected (500 °C, 2 h). The reduced BFS was denoted as BFS-R, while the leached and H_2-reduced sample was named BFS-L-R.

2.4. *Catalytic tests*

The catalytic activity of the activated BFS samples (BFS-L-R) was measured for the CO hydrogenation reaction to produce methane (CH_4). The runs were carried out in a laboratory fixed bed reactor (OD: 9.5 mm L: 500 mm) made of stainless steel, equipped with mass flow controllers (BROOKS 5850E) and connected to a gas chromatograph PERKIN-ELMER (model Clarus 580), which contains a FID with methanizer and a Porapak Q column (1.82 m length, 2.1 mm diameter) operating at 350 ºC. The reaction was carried out at 300 – 380 ºC and 1 bar, with variable H_2/CO ratios and a total flow of 100 ml/min, using N_2 as a balance gas. Although methane formation is favored at higher pressures, thermodynamic equilibrium calculations [49] have shown that, at lower temperatures (<400 °C), pressure does not affect neither CO conversion nor methane selectivity. Thus, atmospheric pressure was selected for experimental simplicity.

At all cases, 300 mg of catalyst sample was charged to the reactor to ensure differential regime (i.e., CO conversion < 10 %). Before reaction, the BFS sample was reduced under H_2 at 500 ºC for 2 h, conditions selected from the results of reducibility tests (section 2.3.2). Partial pressures of H_2 and CO were tuned at 10 – 50 kPa and 0.25 - 3.0 kPa, respectively. Consecutive runs were carried out using different H_2/CO ratios to evaluate the catalytic stability and deactivation. This sequence of experiments finalized by repeating the first condition (H_2/CO=20:1). In all cases, reaction time was selected until a stable trend was observed. This varied from 12 to 18 h, and reported results correspond to mean values of the last 4 h. This high H_2/CO ratio (20:1) was selected for the kinetic study in order to favor methane formation [49] and to avoid carbon deposition and higher hydrocarbons formation.

The Weisz-Prater and Mears criteria [50] were applied at the higher tested temperature for the active catalyst that shows higher CO conversion rate, to rule out intra- and extra-particle mass transport limitations, respectively (see Supplementary Information). Experimental runs were kept until steady state conditions were achieved. Heat transfer effects are negligible under the assayed conditions, i.e. highly diluted gases (with He as inert gas) and low CO conversions (because of the differential regime). This is also confirmed by the Mears criterion (see Supplementary Information). Reaction

parameters were calculated from the product analysis. These were: CO conversion (%), rate of CH_4 formation (mmolCH_4/g_{cat}·min), and selectivity to CH_4 (%).

To study the effect of SO_2, a BFS sample of 150 mg was treated with SO_2 (200 ml/min of SO_2 diluted in N_2, to range 5000-15000 ppm concentration), at 350 ºC for 2 h (heating rate of 5 ºC/min). The doping was done in a TGA system, Netzsch STA 409 Luxx. After this, the sample was located in the catalytic system, reduced in H_2 and tested for its catalytic performance at 350 ºC, following the procedure described above. Rates of methane formation were determined and compared to that of the SO_2-free catalyst.

3. Results and Discussion

3.1.1. BFS Characterization

BFS is an industrial waste that requires a proper activation treatment before being used as a catalyst for CO reduction. This pretreatment was divided into two stages: a purification stage that targets the elimination of the components that will affect selectivity to methane, and the reduction stage to activate Fe that is found in the BFS in different mineral forms. To corroborate the effectiveness of the applied treatment the sample was characterized as described in section 2. In all cases, particle size in the range 106 – 150 µm were considered. A preliminary study demonstrated that, in this range of particle size, concentrations of elements like S and C showed the lowest values (see Supplementary Information). In other words, these undesired species are more abundant in the fine fractions.

Concentration of major elements in the leached sample compared to the original one (fresh BFS) is shown in Table 1. The main components in the BFS are Fe, C and Ca, which are constituents of the raw materials, iron ore, coke, and limestone, fed into the blast furnace for steel production.

Table 1: Average concentration of major elements in BFS and BFS-L.

Element (wt.%)	BFS	BFS-L
Fe	47.08	51.68
Ca	2.61	0.23
Mg	0.59	0.39
Zn	0.31	0.03
Mn	0.10	0.08
K	0.04	0.01
Ni (ppm)	<3.0	< 3.0
C	11.81	13.85
S	0.17	0.13

Results of Table 1 confirm the effectiveness of the leaching treatment aimed at reducing the concentration of all the accompanying elements, especially calcium and potassium. This last element is known for its promoting effect on the reactions that leads to the formation of higher molecular weight hydrocarbons [27, 28]. Besides SiO_2 (5.22 wt. %) and Al_2O_3 (2.03 wt.%), other elements present in the BFS (detected by X-ray fluorescence) showed concentrations less than 1 wt. %.

During reduction, carbon generates some methane by direct hydrogenation. However, this phenomenon is negligible as shown by the stability tests carried out in the differential reactor (see Section 2.4).

Figure 1 shows the TG-MS results of reducibility tests using H_2 as a reducing gas. According to Oliveira et al. [51] and Jozwiak et al. [52] the reducibility profile of pure hematite presents two peaks: a first peak in the range 300 – 400 °C, related to the reduction of hematite to magnetite ($3Fe_2O_3+H_2 \rightarrow 2Fe_3O_4$), and a second peak at 570 – 700 °C, that represents reduction of magnetite to metallic iron ($2Fe_3O_4+8H_2 \rightarrow 6Fe$). For the BFS sample, two peaks are also observed (Figure 1).

The first one, begins at 400 °C (first peak) and finishes at about 500 °C. Reduction of Fe_2O_3 to Fe_3O_4 is corroborated by the H_2O signal detected by MS in this temperature range. Also a partial reduction of Fe_3O_4 to Fe occurs. The calculated weight loss during BFS reduction (23.3 %) agrees well with that calculated from the hematite/magnetite-, magnetite/Fe- contents and the stoichiometry of the

above reduction reactions (3.3 % and 27.6 % for Fe_2O_3 to Fe_3O_4 and Fe_3O_4 to Fe respectively), confirming the occurrence of magnetite reduction to Fe^0 in the BFS sample near 500 °C. Methane formation is also shown in Figure 1. This is observed at approximately 600 °C (second peak) and it comes from carbon present in the BFS sample but, as we show later in Figure 6, has no influence during the catalytic tests. In fact, Figure 6 shows that the methane formation observed during BFS reduction at approximately 600 °C (Figure 1) is attributed to the carbon present in the BFS sample (Table 1). However, this resulted negligible as compared with the methane formation observed at H_2/CO 20:1 on the activated BFS catalysts (Figure 6). From these results, reduction temperature and time of 500 °C and 2 h, respectively, were selected as pretreatment conditions.

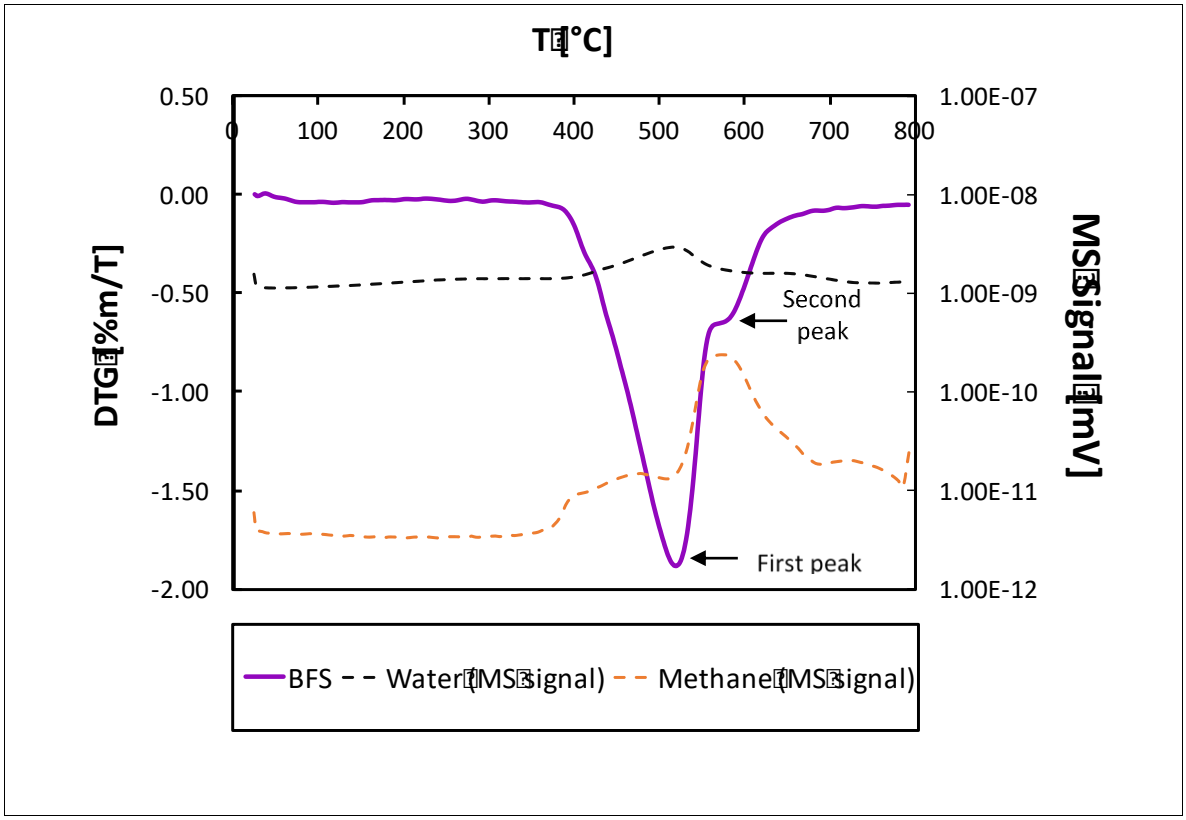

Figure 1. H_2- reduction of BFS by TGA coupled to MS. (800 °C, 80 ml H_2/min, 10 °C/min)

The XRD pattern (Figure 2) of BFS shows that the major iron mineral is hematite (Fe_2O_3). To a lesser extent, iron is also present as magnetite (Fe_3O_4). Calcite ($CaCO_3$) and carbon were also identified but in a much less proportion. The presence of calcite can be associated with limestone, added to the

blast furnace to produce blast furnace slag [53]. As mentioned, carbon results from the residual metallurgical coke fed to the blast furnace as a reducing agent in steel production. The observed proportions of Fe/Ca, Fe/C and Fe/Si agree well with published results [44, 53-56]. Figures 3 and 4 show the XRD patterns from the in situ-XRD assays. According to this, the reduction of Fe_2O_3 to Fe_3O_4 in the BFS starts at 450 ºC (Figure 3), but the peak of metallic Fe is detected above 500 ºC together with the magnetite phase, and they remain even after cooling the system to room temperature (under H_2 atmosphere). Thus, the Fe + Fe_3O_4 phases turned out to be stable at these conditions. However, the XRD of hematite (Figure 4) shows that its reduction to magnetite occurs from 350 ºC and this, subsequently, reduces to wüstite (FeO), a transformation that starts at 600 ºC and finishes with the complete conversion of Fe_3O_4 to FeO, at 800 ºC.

It should be noted that in the studied temperature range (300 – 800 ºC) no metallic Fe was detected during reduction of the hematite standard.

H_2 reduction of hematite is a gas-solid heterogeneous reaction that can be represented by the shrinking core model [57]. As reduction proceeds, the unreacted hematite core shrinks and it is surrounded by a layer of reaction products (the ash layer). Hydrogen diffuses through the product layer to reach the reaction front located at the boundary between the core and the product layer. The reduction rate is initially controlled by the interfacial reaction on the core surface and, as reduction proceeds, diffusion of H_2 through the growing layer becomes the rate-controlling step. In the case of BFS, because of the lower concentration of hematite, and thus higher presence of an ash layer formed by inert material, the reduction rate would be controlled by the diffusion of hydrogen from the beginning of reaction. This would explain the shift to higher temperatures (Figure 4), and the absence of metallic Fe (Figure 3) observed during reduction of the BFS and the hematite standard, respectively.

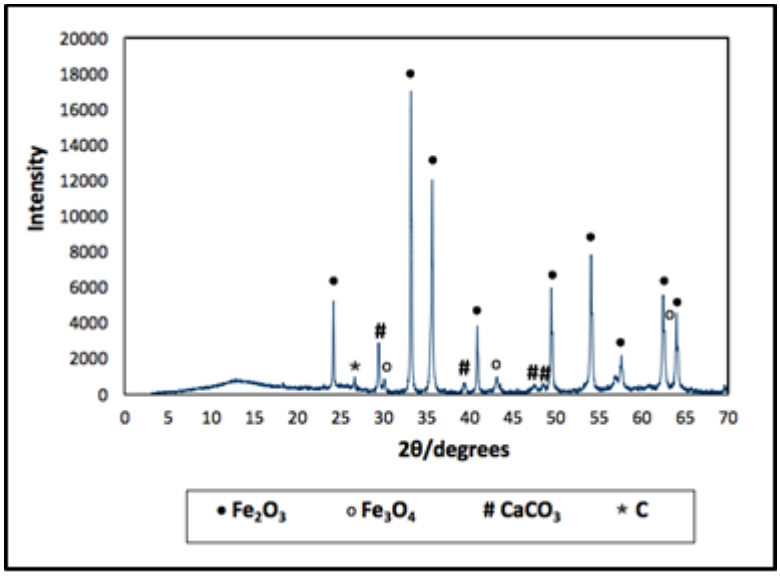

Figure 2. X-ray diffraction patterns of BFS.

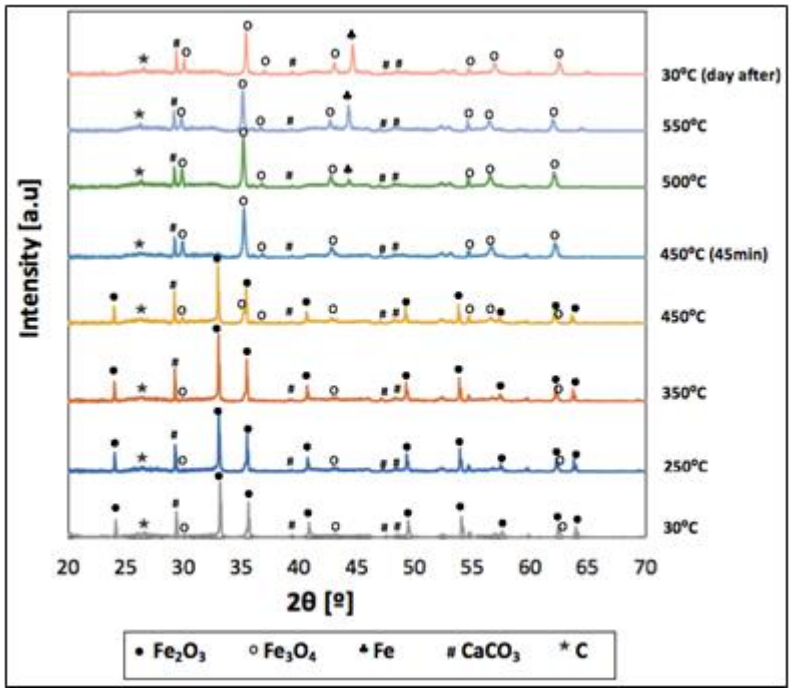

Figure 3. In situ X-ray diffraction patterns of BFS. (10 ml/min, 10 %H_2/Ar)

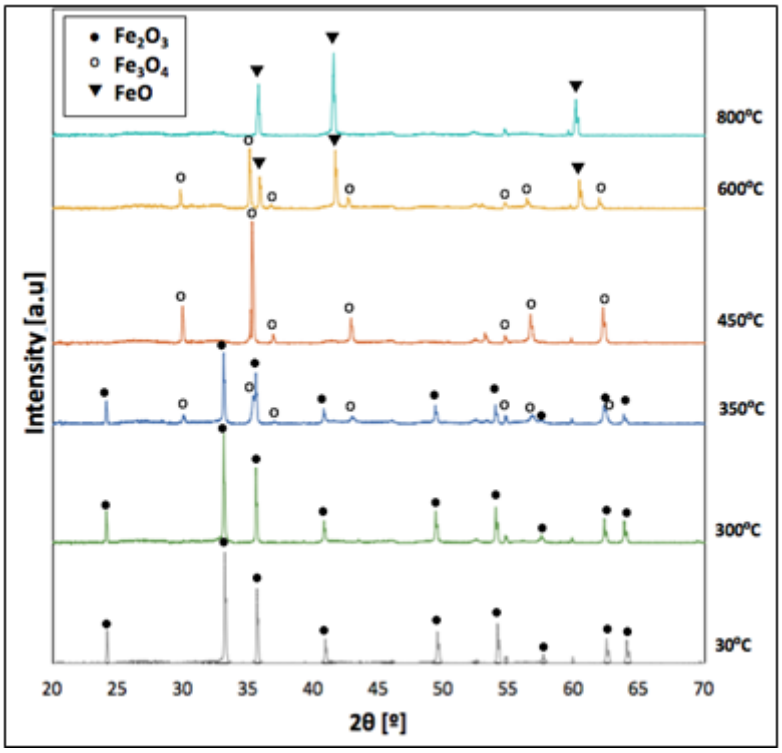

Figure 4. In situ X-ray diffraction patterns of standard hematite. (10 ml/min, 10 %H_2/Ar)

Regarding surface area, as expected, N_2 adsorption analysis of BFS showed very low values (3.8 m^2/g), with average pore sizes of 14.6 nm. Amorim et al. [56] and Gao et al. [58] reported similar results. The low specific surface area of the material causes a low dispersion of the Fe-phases (active sites) on the catalytic surface, due to their larger particle size. Although a greater dispersion would represent a greater number of surface active sites, it has been reported that for the CO methanation reaction, the intrinsic activity of transition metals increases with particle size [59]. Furthermore, these larger particles, with a high degree of sintering, are more stable than the smaller ones, which tend to sinter at operating temperatures.

3.3. Catalytic tests

Table 2 shows the results for CO conversion (%), CH_4 formation and selectivity (%), obtained during the catalytic tests.

Table 2. Catalytic activity and selectivity for CO hydrogenation. (T= 320ºC; H_2/CO = 20:1).

Sample	%CO Conversion	%CH_4 Selectivity	$CH_4 \cdot 10^3$ (mmol/gcat·min)	%CO_2 Selectivity	%C^{2+} Selectivity[a]
BFS	3.1	15.8	0.73	31.2	53.0
BFS-R	8.7	23.9	3.22	11.2	64.9
BFS-L-R	3.5	49.5	2.63	18.0	32.5

[a]: Hydrocarbons with two or more carbon atoms.

Results of Table 2 show the favorable effect of the applied activation procedures (leaching and reduction) on the methane selectivity, which increases from 15.8 % to 49.5 %. Other products are CO_2 and C^{2+} hydrocarbons. Figure 5 shows the evolution of methane formation rate with reaction time. For both samples, BFS-R and BFS-L-R, the reaction rates achieve their highest values during the first minutes, then the reaction rate diminishes and achieves a trend close to “steady state” which remains apparently constant showing no signs of deactivation. These are rhe values reported in Table 2. This initial behavior has been observed by other authors [60] and has been attributed to the rapid carburization of the catalyst surface. In our case, due to the stability showed during the consecutive assays (see Figure 6), we suggest for the activated samples (BFS-R and BFS-L-R) that, at the beginning of the reaction a gradual filling of CO* species on surface occurs until stabilization is achieved, at the same time that CH_4 is produced. Another important behavior is the stability of the material and its resistance to deactivation, at least under the reaction conditions selected in this study. Rate of methane formation obtained in this work for BFS-L-R is 0.00263 mmolCH_4/gcat/min,@320°C,1bar, and H_2:CO=20:1. Using nickel-based catalysts, Yue Yu et al., derived a kinetic expression from whose parameters a value of 0.0038 mmol CH_4/gcat/min can be calculated for 320 °C and 1 bar [70]. However, other authors [71] have achieved different values, probably because of the higher selectivities (to methane) exhibit by nickel.

XPS results shown in Table 3 demonstrate that BFS-L has a higher Fe content and a slightly lower carbon content on its surface compared to the original BFS sample. The removal of Ca and Zn from the surface after the leaching is also shown. This result could explain the higher CO conversion for the BFS-R compared to the BFS-L-R (Table 2). Nakhaei et al. [61] evaluated the effect of Ca, La and Mg as promotors in the FTS using Fe/SiO_2 catalysts. They observed an increase in CO conversion as a function of the catalyst basicity, particularly following the trend Ca>Mg>La>not promoted and concluded that high basicity of the catalysts restrained the hydrogenation and CH_4 production as well as favored the selectivity to olefins.

On the other hand, Li et al. [62] studied the effect of Zn in Fe catalysts promoted by K and Cu in FTS, reporting that high contents of Zn in the catalyst favored CO conversion. Then, when Zn/Fe was increasing in the range 0.1 – 0.4, there was an increase in activity to hydrocarbon formation rate and selectivity to CH_4. As shown in Table 3, the Zn/Fe ratio in our BFS is 1.2, that is, higher than the spectra chosen of Li et al. This could explain the higher activity, but lower selectivity to CH_4, of the BFS sample in comparison to the BFS-L-R (Zn/Fe=0). This result could also be attributed to the higher Si/Fe and Al/Fe ratios in the BFS compared to those of BFS-L. It has been reported that Al and Si are structural promoters for Fe catalysts in FTS reaction, due to the strong metal-support interactions [63, 64]. In our case, lower Al/Fe and Si/Fe obtained in BFS-L after the leaching treatment and H_2 activation, favored selectivity to CH_4 due to a decrease in the structural interactions with the superficial Fe. From the values of table 3, a first approximation gives $2.51 \cdot 10^{-2}$ and $4.24 \cdot 10^{-2}$ mmolCH_4/molFe/min for BFS and BFS-L respectively, which demonstrates the favorable effect of this element. If the catalyst surface were higher, surface Fe could be increased and with it, catalytic activity. This can be achieved by using a high-surface-area compound (SiO_2 for example) as a support for BFS or even by using BFS/SiO_2 blends. Alternatively, BFS-L could be submitted to further chemical (acid digestion) or thermal pretreatments. Thus, further work is still needed in order to optimize the catalyst surface area and its properties.

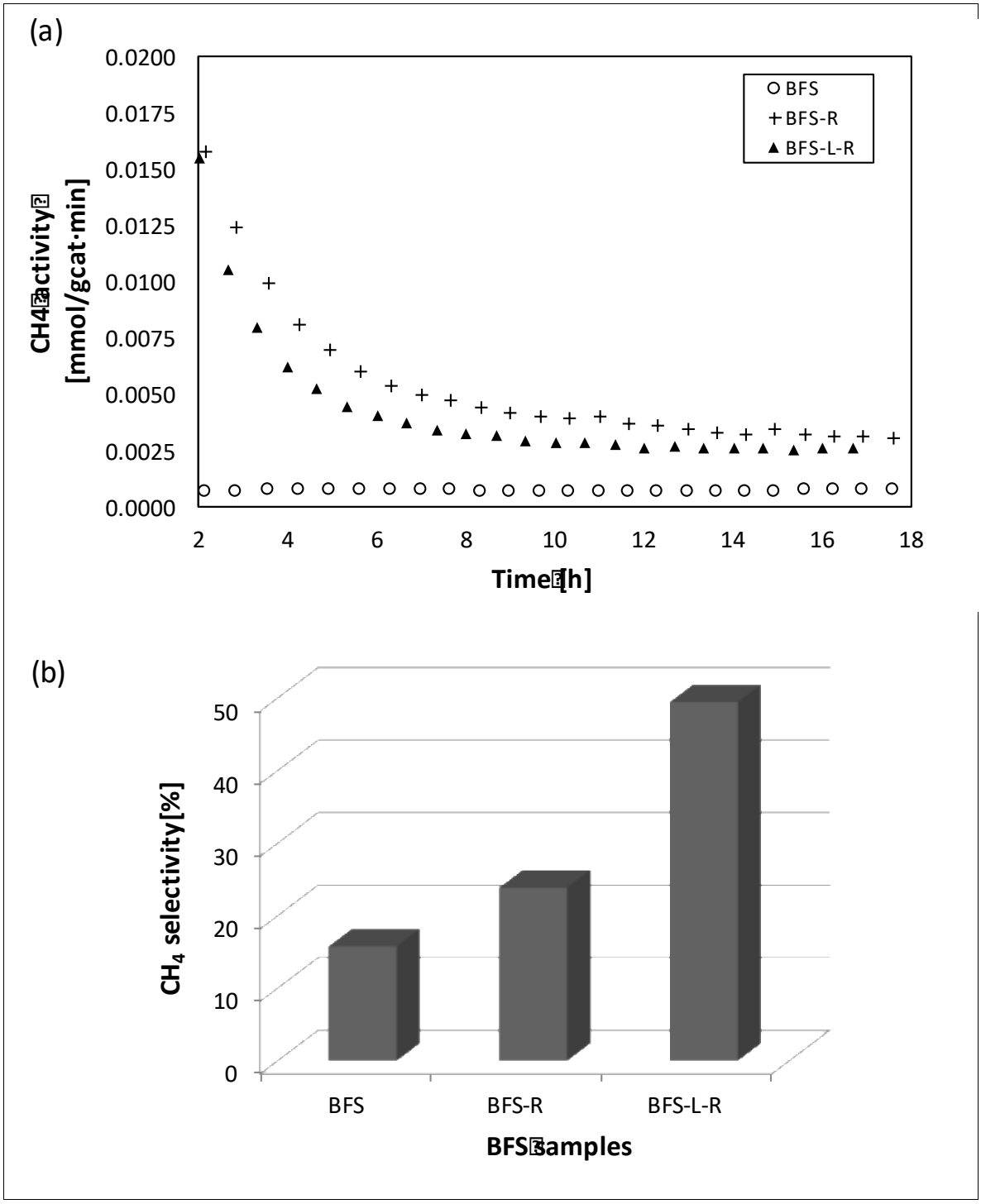

Figure 5. (a) Rate of CH_4 formation (mmolCH_4/gcat·min) as a function of reaction time; (b) CH_4 selectivity during CO methanation using BFS, H_2-reduced BFS (BFS-R), BFS leached and reduced in H_2 (BFS-L-R) ($T_{reaction}$= 320 °C, 100 ml/min H_2:CO=20:1).

Table 3. Molar concentration of surface elements in BFS, BFS-L and hematite standard measured by XPS.

Sample	Fe (%)	Ca (%)	Ca/Fe	Zn (%)	Zn/Fe	Si (%)	Si/Fe	Al (%)	Al/Fe	C (%)	O (%) balance
BFS	2.9	2.5	0.9	3.6	1.2	6.2	2.1	2.8	1.0	46.3	35.7
BFS-L	6.2	0	0	0	0	5.8	0.9	1.5	0.2	34.9	54.9
Hematite	19.2	0	0	0	0	0	0	0	0	29	51.8

3.4. Kinetic model

CO methanation was carried out at 320 ºC and 350 ºC tuning the H_2/CO ratio in the ranges $0.5<P_{CO}<3.0$ kPa and $10<P_{H2}<50$ kPa using BFS-L-R as a catalyst. Figure 6 shows that the catalyst resulted stable under the reaction conditions selected without signs of catalytic deactivation, as confirmed by reproducibility of methane formation rate after 170 h of reaction (see results at the first and last H_2/CO= 20:1 condition).

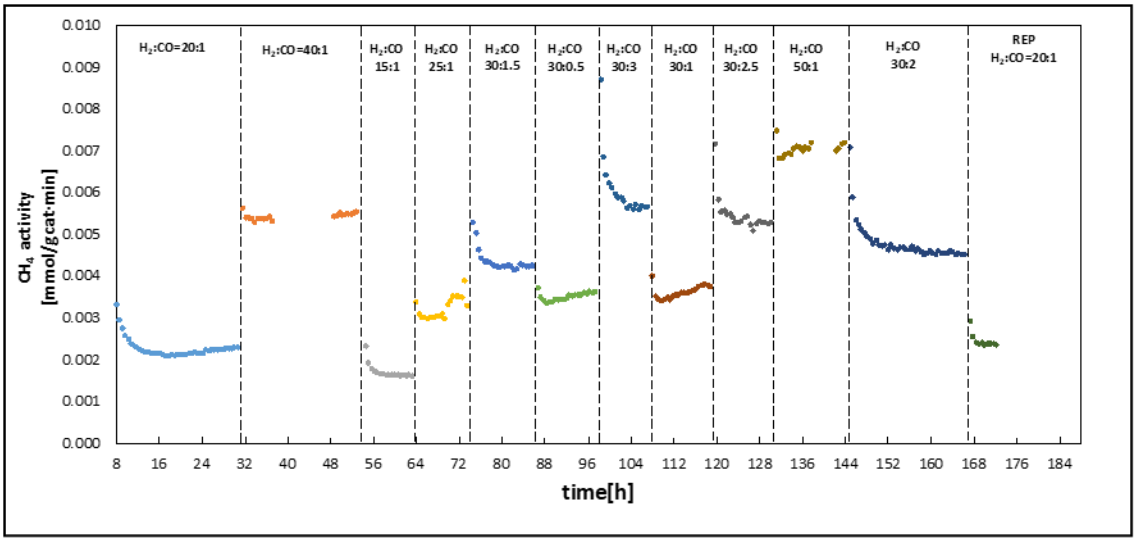

Figure 6: Consecutive catalytic tests of CO hydrogenation at variable H_2/CO ratios using BFS-L-R as a catalyst (T=320 °C, 100 ml/min).

Figures 6 and 7 show the effect of H_2 and CO partial pressure on CO consumption and selectivities to CH_4 and CO_2 at 320 ºC and 350 ºC. In all cases, CO conversion was less than 10 % thus confirming

the existence of a differential regime (see Supplementary information). At P_{CO} equal to 0.9 kPa, a linear correlation between the rate of CH_4 production and P_{H2} (Figures 7-a and 7-b) and no influence of P_{H2} on CO_2 production rate is observed. In the case of variable P_{CO} (Figures 7-c and 7-d), in the range studied, a more favorable effect of P_{CO} on CH_4 formation, compared to CO_2, is observed, which demonstrates a slight domain of the methanation reaction over the water gas shift. However, this trend may change for higher P_{CO} values, as observed at 350 °C (Figure 7- c) where the slope of the CO_2 formation rate is higher than that of methane production. In any case, the low values of approach to equilibrium, calculated for the WGS at the highest assayed temperature, (6.5 to $9.5 \cdot 10^{-2}$, see supplementary information) confirm the absence of thermodynamic limitations.

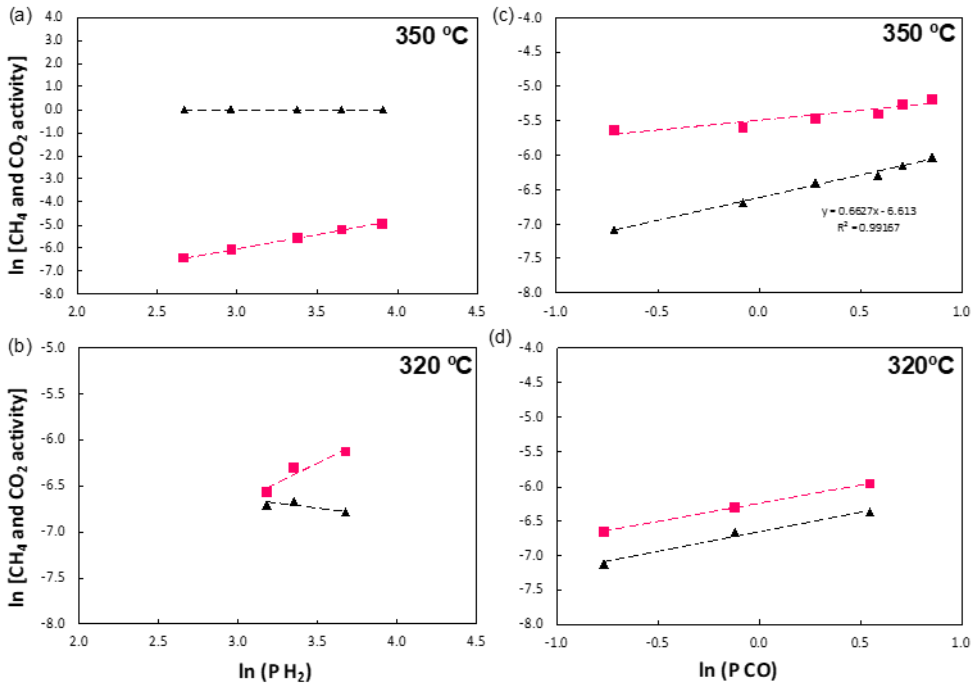

Figure 7. a) Effect of partial pressure of H_2 (P_{CO} = 0.9 kPa) on catalytic activity at: a) 350 ºC, (b) 320 ºC. Effect of partial pressure of CO (P_{H2} = 29.0 kPa) on catalytic activity at: c) 350 ºC, (d) 320 ºC. ■ ln(CH_4 activity), ▲ ln(CO2 activity), --- ln(CH_4 activity), --- ln(CO_2 activity).

From these results, a sequence of elementary steps is proposed in Figure 8, and derived Langmuir-Hinshelwood kinetic models for the CH_4 and CO_2 production rates are used to fit the kinetic data. Because of the very low conversions (conditioned by the differential regime) only the forward reaction

rates were considered for the analysis. Thus, for higher conversions, the inclusion of the corresponding reverse reactions should be considered.

Rate expressions for CH_4 and CO_2 production in terms of CO and H_2 partial pressures are proposed (see Table 5). The second addition of H* to form the HCOH* intermediate (step 4, Figure 8) was considered the rate-limiting step for the CH_4 production (Eq.4 in Table 6). A kinetic expression for CO_2 formation by the WGS reaction is also adjusted by considering step 6 as the kinetically relevant, that is, CO* dissociation to C* and O* unassisted by H*. Besides, CO* coverage and empty sites were considered as the predominant surface species. These suppositions are supported by the work of Ojeda et al. [36, 37] who, through theoretical and experimental studies, showed that the elementary steps for the Fischer-Tropsch reaction in Fe catalysts follow two parallel routes for CO dissociation (with and without H assistance).

1.	$CO + {}^* \rightleftharpoons CO^*$	K_1
2.	$H_2 + 2^* \rightleftharpoons 2H^*$	K_2
3.	$CO^* + H^* \rightleftharpoons HCO^* + {}^*$	K_3
4.	$HCO^* + H^* \rightarrow HCOH^* + {}^*$	k_4
5.	$HCOH^* + {}^* \rightarrow CH^* + OH^*$	k_5
6.	$CO^* + {}^* \rightarrow C^* + O^*$	k_6
7.	$C^* + H^* \rightarrow CH^* + {}^*$	k_7
8.	$CH^* + H^* \rightarrow CH_2^* + {}^*$	k_8
9.	$CH_2^* + H^* \rightarrow CH_3^*$	k_9
10.	$CH_3^* + H^* \rightarrow CH_4^* + {}^*$	k_{10}
11.	$OH^* + H^* \rightarrow H_2O + 2^*$	k_{11}
12.	$CO^* + O^* \rightarrow CO_2 + 2^*$	k_{12}

Figure 8: Elemental steps proposed for the CO methanation using BFS-L-R as a catalyst.

On the one hand, the unassisted dissociation of CO allows the production of C* and O* species (step 6), the former react with H* and generate the CH* species (step 7) while O*, when reacting with CO*, generates CO_2 (step 12, Figure 8). On the other hand, the assisted dissociation of CO involves the

formation of CH* species and OH*, the latter being responsible for H_2O production (step 11). Successive hydrogenation steps of CH* species (steps 9 and 10) lead to methane formation.

Thus, the expression of methane production (Eq. 4) was defined considering the second addition of H* to the intermediate HCO* as a kinetically relevant step (step 4, Figure 8), while the first addition of H* to the intermediate HCO* was considered as a quasi-balanced step (step 3, Figure 8). Both CO* and H* were obtained from adsorption equilibria of the respective surface gases CO and H_2 (step 1 and 2 respectively, Figure 8). The result is a Langmuir-Hinshelwood expression that considers the partial pressure of CO and H_2 in the numerator of the equation, which demonstrates the effect of both reactive gases on methane production already discussed in Figure 7.

On the other hand, a rate law for CO_2 production (Eq. 5), which only depends on the partial pressure of CO (see Figure 7), was derived considering the non-assisted dissociation of CO* as a kinetically relevant step (step 6, Figure 8), where the CO* species were obtained by step 1 (Figure 8) representing the equilibrium adsorption of CO on the catalytic surface.

To verify the accuracy of the prediction based on the experimental data, the Mean Absolute Relative Residual (MARR) was evaluated. This criterion is defined by the following expression:

$$MARR\ (\%) = \sum_{i=1}^{N_{exp}} \left| \frac{r_{exp} - r_{adj}}{r_{exp}} \right| \text{x} \ \frac{1}{N_{exp}} \ \text{x}100 \qquad \text{(Eq.3)}$$

Where r_{exp} and r_{adj} represents rate values calculated experimentally and those obtained by the selected model, respectively. N_{exp} corresponds to the number of data considered for the adjustment. The kinetic models and parameters adjusted at 350 °C are shown in Table 5. Figure 9 shows the resulting parity plots.

Table 5. Langmuir – Hinshelwood models and kinetic parameters for CO methanation.

L-H models	Kinetic parameters at T= 320 °C	Kinetic parameters at T= 350 °C
$r_{CH_4} = \frac{k_4 K_1 K_2 K_3 P_{H_2} P_{CO}}{(1 + K_1 P_{CO})^2}$ (Eq. 4)	$k_4 K_1 K_2 K_3$ = 1.0409·10^{-4} mmolCH_4·kPa^{-2}·gcat^{-1}·min^{-1} K_1 = 0.2679 kPa^{-1} **MARR = 8.06%**	$k_4 K_1 K_2 K_3$ = 1.7216·10^{-4} mmolCH_4·kPa^{-2}·gcat^{-1}·min^{-1} K_1 = 0.1514 kPa^{-1} **MARR = 12.70%**
$r_{CO_2} = \frac{k_6 K_1 P_{CO}}{(1 + K_1 P_{CO})^2}$ (Eq. 5)	$k_6 K_1$ = 2.0954·10^{-3} mmolCO_2·kPa^{-1}·gcat^{-1}·min^{-1} K_1 = 0.2679 kPa^{-1} **MARR= 4.47%**	$k_6 K_1$ = 1.8242·10^{-3} mmolCO_2·kPa^{-1}·gcat^{-1}·min^{-1} K_1= 0.1514 kPa^{-1} **MARR = 5.29%**

Results of Figure 9 and Table 5 confirm the feasibility of Langmuir-Hinshelwood models to represent the kinetics of CO methanation using BFS-L-R as a catalyst. Additionally, the apparent activation energy for the CH_4 formation rate was calculated in the range of 320 – 380 ºC. The obtained value was 93.2 kJ/mol (Figure 10), which is comparable to those reported in the literature for methane formation from CO hydrogenation [65, 66].

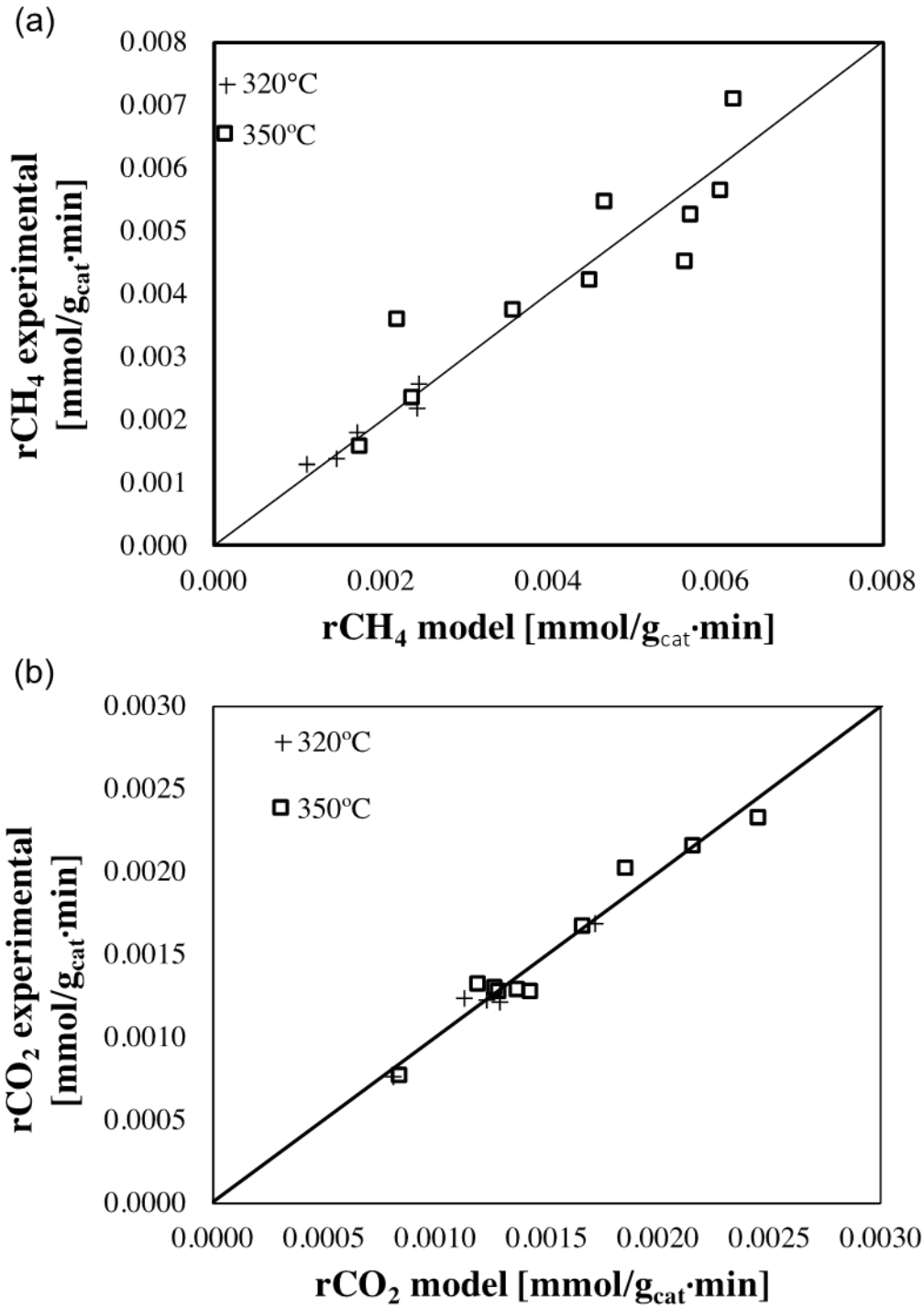

Figure 9. Parity plot for the CO methanation using BFS-L-R as a catalyst at 320 ºC and 350 ºC for (a) CH_4 and (c) CO_2 activity.

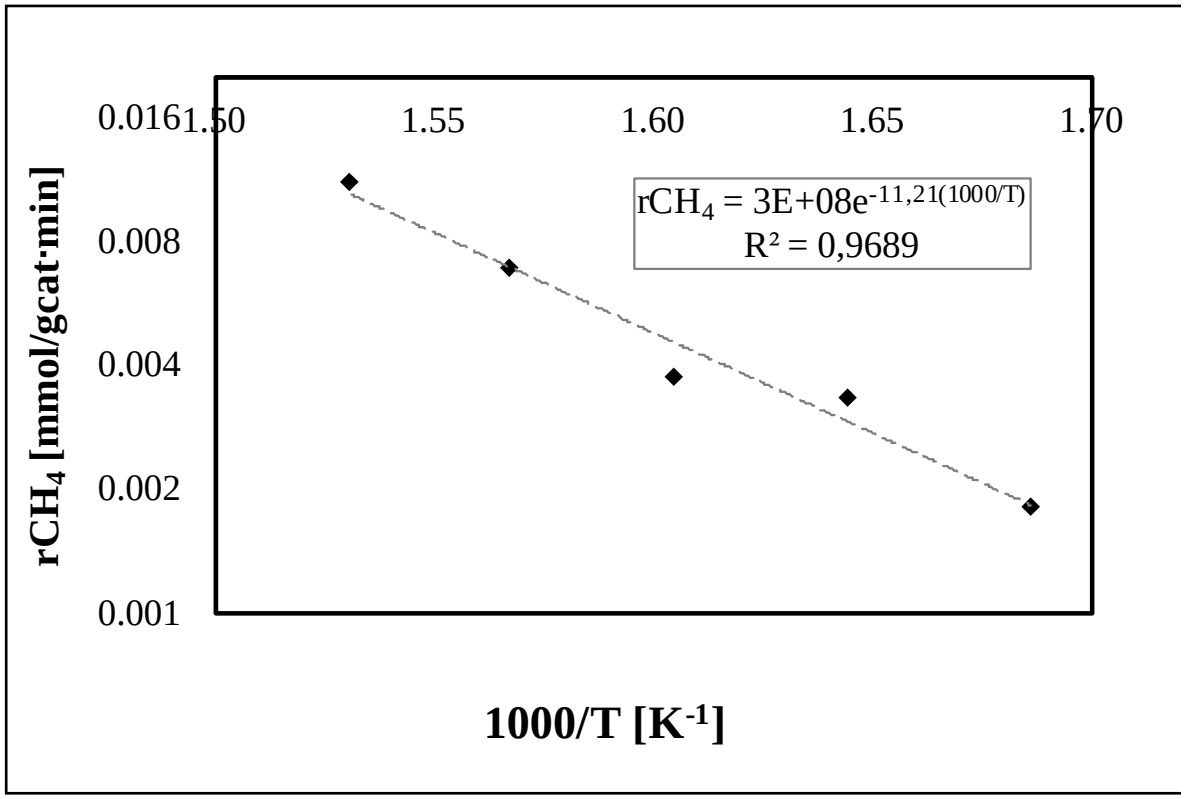

Figure 10. Arrhenius plot for the CH_4 formation rate using BFS-L-R as a catalyst (Total flow: 100 ml/min H_2:CO=30:1)

3.6. Effect of SO_2 in the CH_4 activity and selectivity

Results of catalytic behavior after SO_2 pretreatment of the catalyst BFS-L-R are shown in Fig.11-a. Prior to the catalytic tests, the sample was activated with H_2. It should be noted that most of the studies on catalytic deactivation by sulfur use concentrations in the feed gases in the order of 10 ppm [67, 68]. Therefore, an attack of 15000 ppm of SO_2 is an excellent indicator to demonstrate the stability and resistance to sulfur poisoning of the catalyst synthesized from a steel waste. As expected, a slight catalytic deactivation is observed. Methane formation decreases in a more or less exponential way with SO_2 concentration. A deactivation function is proposed to describe this behavior, (Eq. 6).

$$-r_{CH_4} = \Phi(SO_2) \cdot r_{CH_4SD} \quad \text{(Eq.6)}$$

$\Phi(SO_2)$ corresponds to the deactivation function of the CO methanation, which depends on the SO_2 concentration, and r_{CH_4SD} corresponds to the modeled reaction rate without deactivation (Table 5). To develop an expression for this SO_2 deactivation, first-order deactivation kinetics with respect to the total surface sites, L, was assumed (Eq. 7):

$$\Phi(SO_2) = \frac{dL}{dC_{SO_2}} = \beta \cdot L \quad \text{(Eq.7)}$$

Integrating:

$$L = L_0 e^{-\beta C_{SO_2}} \quad \text{(Eq. 8)}$$

L_0 represents the total of sites available for CH_4 production, without the effect of SO_2. On the other hand, β represents a constant, which depends on the nature of the catalyst, the reaction conditions and type of pretreatment, among others. Data are fitted assuming proportionality between the CH_4 production and the number of available sites (L). The result is shown in Fig.11-c.

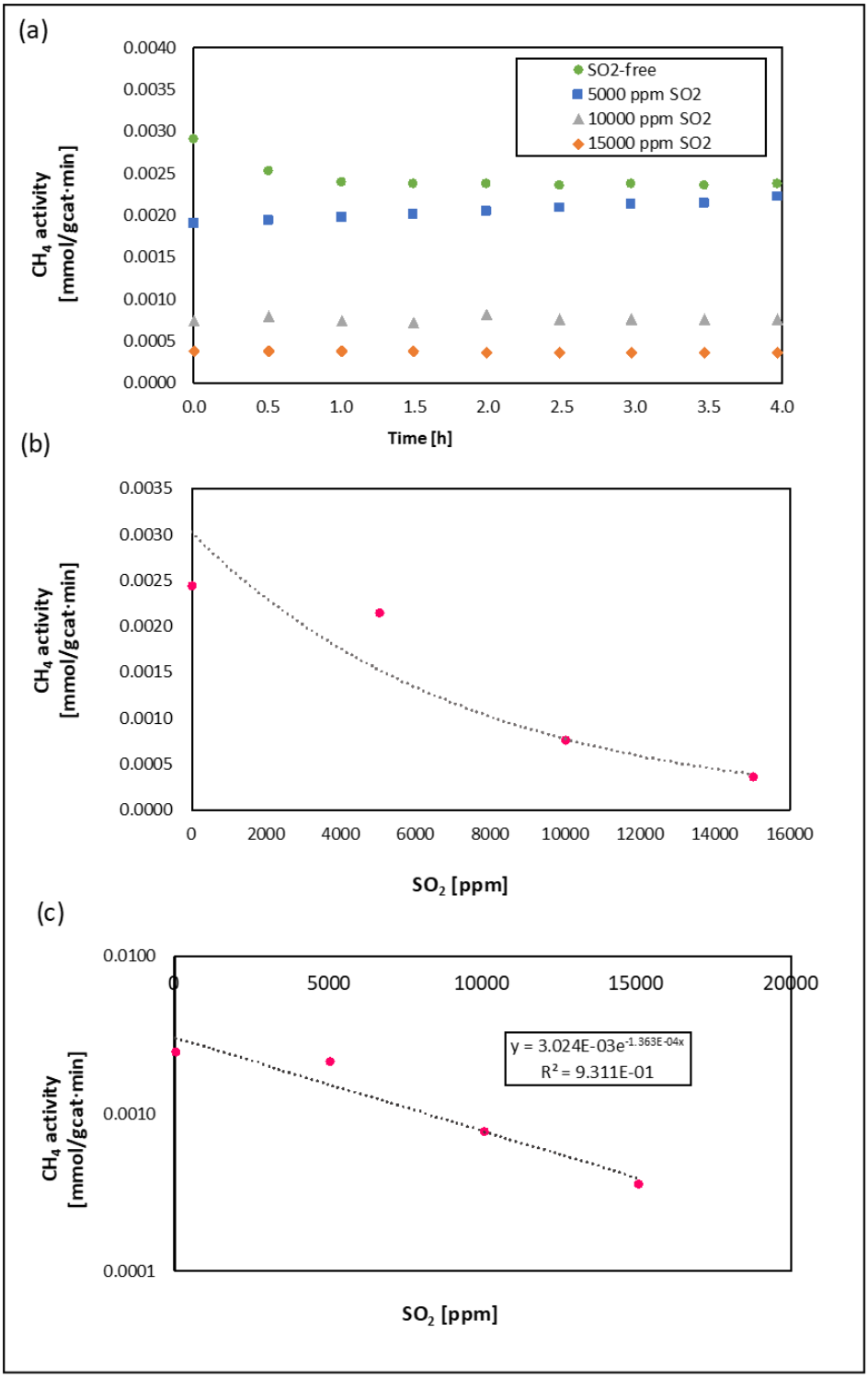

Figure 11. Effect of SO_2 poisoning on BFS-L-R catalyst during CO hydrogenation. (a) Methane formation rate as a function of reaction time, (b) Methane formation rate as a function of SO_2 concentration used during pretreatment. ● SO_2-free, ■ 5000 ppm SO_2, ▲10000 ppm SO_2, ◆ 15000 ppm SO_2. (c) Ln r_{CH4} vs C_{SO2}. Experimental data, deactivation model (···).

Commercial catalysts normally used for CO hydrogenation, require concentrations lower than 15 ppb of H_2S (0.028 ppm of SO_2) in the feed stream. It has been demonstrated [69] that exposure of a nickel catalyst to H_2S concentrations in the range 15-100 ppb (0.028 - 0.188 ppm SO_2) generates loses in its CH_4 activity from one to four orders of magnitude. Our results, however, demonstrate the resistance of the BFS-L-based catalyst against SO_2, which combined with the kinetic model, would confirm its resistance to poisoning when sulfur is present in the feed. Ongoing work is oriented to this objective.

4. Conclusions

Blast Furnace Sludge (BFS), a waste of the steelmaking industry, sieved, leached (L) and reduced (R) in H_2, constitutes an interesting material suitable for its use as a Fe based catalyst in the CO methanation reaction. The results showed that treated BFS (BFS-L-R), rich in Fe and with lower contents of Ca and K, exhibited a satisfactory catalytic activity and CH_4 selectivity. The kinetic behavior under the studied conditions can be represented by a Langmuir-Hinshelwood (L-H) kinetic model that considers both, CH_4 and CO_2 formation, at the operating range of P_{CO} 0.25 - 3.0 kPa, P_{H2} 15 – 50 kPa and temperatures 320 ºC – 350 ºC. This L-H model is derived from a sequence of elementary steps, which consider that H_2-assisted CO dissociation leads to CH_4 formation, while the unassisted path explains CO_2 formation.

The effect of SO_2 poisoning on the CH_4 formation rate was also studied. Results showed a slight inhibiting effect on catalytic activity, which can be described by a first-order model with respect to all available sites on the surface, resulting in an exponential decrease in CH_4 catalytic activity as a function of the SO_2 concentration. The catalyst showed a very stable behavior after 170 h of continuous operation at different reaction conditions. The results presented in this study offer a new approach for the use of an available low-cost and Fe-rich waste to produce active catalyst for SNG production. A contribution to a more sustainable catalysis.

Acknowledgements

This work was supported by Conicyt (Chile), FONDEF Project N° ID15I10247 and FONDECYT 1170610. Authors are profoundly thankful to Compañía Siderúrgica Huachipato (Huachipato Steel Company), Chile, for the provision of waste materials that have been used in this work. The authors would also like to thank Ing. Marcela Saavedra and Chem. Assistant Mrs. Verónica Sierra for the assistance in the experimental work. F.R.S.–F.N.R.S. is also thanked for the acquisition of the in situ XRD equipment (project EQP UN00616F).

References

1. Cheng, C., Shen, D., Xiao, R., Wu., C.,Methanation of syngas (H_2/CO) over the different Ni-based catalysts, Fuel 2017; 189:419-427.
2. Alhajeri, N.S., Dannoun, M., Alrashed, A., Aly, A.Z., Environmental and economic impacts of increased utilization of natural gas in the electric power generation sector: Evaluating the benefits and trade-offs of fuel switching, Journal of Natural Gas Science and Engineering 2019; 71: 102969.
3. Cristescu, T., Stoica, M.E., Suditu, S., Research on th Carbon Dioxide Emission Factors as a Result of Fuel Combustion", Rev. Chim. (Budapest) 2019; 70 (2), 585-590.
4. IEA (2019), "Global Gas Security Review 2019", IEA, Paris https://www.iea.org/reports/global-gas-security-review-2019.
5. Lebarbier, V.M, Dagle, R.A., Kovarik, L., Albrecht, K.O, Li, X., Li, L., Taylor, Ch.E., Bao, X.,Wang, Y., Sorption-enhanced synthetic natural gas (SNG) production from syngas: A novel process combining CO methanation, water-gas shift, and CO_2 capture, Appl. Catal. B: Environmental 2014; 144: 223-232.
6. Gao,J., Liu, Q., Gu, F., Liu, B., Zhong, Z., Su, F., Recent advances in methanation catalysts for the production of synthetic natural gas, RSC Adv. 2015; 5:22759-22776.

7. Liu, Q., Sun, J., Feng, Q., Ji, S., Wang, Z., A La-promoted $Ni/MgAl_2O_4$ catalyst with superior methanation performance for the production of synthetic natural gas, Catal. Today 2020; 339: 127-134.

8. Liu, q., Gao, J., Gu, F., Lu, X., Liu, Y., Li, H., Zhong, Z., Liu, B., Xu, G., Su, F., One-pot synthesis of ordered mesoporous Ni-V-Al catalysts for CO methanation, J. Catal. 2015; 326: 127-138.

9. Kopyscinski, J., Schildhauer, T., Biollaz, S.M.A., Production of synthetic natural gas (SNG) from coal and biomass. A technology review from 1950 to 2009, Fuel 2010; 89: 1763-1783.

10. Gutiérrez-Martín, F., Rodríguez-Antón, L.M., Power-toSNG technology for energy storage at large scales. Int. J. Hydrogen Energy, 2016; 41: 19290-19303.

11. Gu, J., Xin, Z., Tao, M., Lv, Y., Gao, W., Si, Q., Effect of reflux digestion time on MoO_3/ZrO_2 catalyst for sulfur-resistant CO methanation, Fuel 2019; 241: 129-137.

12. Liu, Q., Zhong, Z., Gu, F., Wang, X., Lu, X., Li, H., Xu, G., Su, F., CO methanation on ordered mesoporous Ni-Cr-Al catalysts: Effects of the catalyst structure and Cr promoter on the catalyst properties, J. Catal. 2016; 337: 221-232.

13. Yao, Y., Yu, F., Li, J., Li, J., Li, Y., Wang, Z., Zhu, M., Shi, Y., Dai, B., Guo, X., Two-dimensional NiAl layered double oxides as non-noble metal catalysts for enhanced CO methanation performance at low temperature, Fuel 2019; 255: 115770.

14. Han, Y., Quan, Y., Hao, P., Zhao, J., Ren, J., Highly anti-sintering and anti-coking ordered mesoporous silica carbide supported nickel catalyst for high temperature CO methanation.

15. Mills, G, Steffgen, F., Catalytic methanation. Catal. Rev. 1974; 8: 159-210.

16. Norskov, J. K., Bligaard, T., Rossmeisl, J., Christensen, C. H., Towards the computational design of solid catalysts., Nat Chem. 2009; 1: 37-46.

17. Kustov, A.L., Frey, A.M., Larsen, K.E, Johannessen, T., Nørskov, J.K., Christensen, C.H., CO methanation over supported bimetallic Ni-Fe catalyst: From computational studies towards catalyst optimization. Appl. Catal. A: General 2007; 320: 98-104.

18. Ren, J., Qin, X., Yang, J-Z., Guo, H-L., Lin, J-Y., Li, Z.. Methanation of carbon dioxide over Ni-M/ZrO_2 (M=Fe, Co, Cu) catalyst: Effect of addition of a second metal. Fuel Process. Technol. 2015; 137: 204-211.

19. Pandey, D., Deo, G. Effect of support on the catalytic activity of supported Ni-Fe catalyst for the CO_2 methanation reaction. J. Ind. Eng. Chem., 2016; 33: 99-107.

20. Cheng, J., Zhou, F., Xuan, X., Liu, J., Zhou, J., Cen, K.. Comparison of the catalytic effects of eight industrial wastes rich in Na, Fe, Ca and Al on anthracite coal combustion. Fuel 2017; 187: 398-402.

21. Lu, H., Yang, X., Gao, G., Wang, J., Han, C., Liang, X., Li, C., Li, Y., Zhang, W., Chen, X.. Metal (Fe, Co, Ce or La) doped Nickel catalyst supported on ZrO_2 Modified mesoporous clays for CO and CO_2 methanation. Fuel 2016; 183: 335-344.

22. Li, J., Cheng, X., Zhang, C., Chang, Q., Wang, J., Wang, X., Lv, Z., Dong, W., Yang, Y., Li, Y.. Effect of alkalis on iron-based Fischer-Tropsch synthesis catalyst: Alkali-FeOx interaction, reduction and catalytic performance. Appl. Catal. A: General 2016; 528: 131-141.

23. Wang, D., Chen, B., Duan, X., Chen, D., Zhou, X.. Iron- based Fischer- Tropsch synthesis of lower olefins: The nature of X-Fe_5C_2 catalyst and why and how to introduce promoters. J. Energy Chem. 2016; 25: 911-916.

24. Lo, J.M.H., Ziegler, T., Density functional theory and kinetic studies of methanation on iron surface., J. Physis. Chem. C., 2007; 111: 11012-11025.

25. Andersson, M.P., Bligaard, T., Kustov. A., Larsen, K. E., Greeley, J., Johannessen, T., Christensen, C. H., Nørskov, J. K. Toward computational screening in heterogeneous catalysis: Pareto-optimal methanation catalysts. J.Catal. 2006; 239: 501-506.

26. González, J., Diseño de catalizadores de rutenio para la síntesis de Fischer-Tropsch, in Departamento de Química Física Aplicada.,2012; Universidad Autónoma de Madrid. PhD Thesis.

27. Graf, B., Schulte, H., Muhler, M., The formation of methane over iron catalyst applied in Fischer- Tropsch synthesis: A transient and steady state kinetic study. J. Catal. 2010; 276: 66-75.

28. Yang, J., Ma, W., Chen, D., Holmen, A., Davis, B.H., Fischer- Tropsch synthesis: A review of the effect of CO conversion on methane selectivity. App. Catal. A: General 2014; 470: 250-260.

29. Gaube, J., Klein, H. F., Studies on the reaction mechanism of the Fischer–Tropsch synthesis on iron and cobalt., J. Mol. Catal. A-Chem. 2008; 283: 60-68.

30. Davis, B.H., Fischer–Tropsch synthesis: Reaction mechanisms for iron catalysts., Catal. Today. 2009; 141: 25-33.

31. Satterfield, C.N., Heterogeneous catalysis in industrial practice, 2nd edition. New York, (United States); McGraw Hill Book Co. 1991; None. Medium: X; Size: Pages: (542 p).

32. Fischer, F. and H. Tropsch. Über die direkte Synthese von Erdöl-Kohlenwasserstoffen bei gewöhnlichem Druck. (Erste Mitteilung). Berichte der Deutschen Chemischen Gesellschaft (A and B Series) 1926; 59: 830-831.

33. Maitlis, P.M., A new view of the Fischer-Tropsch polymerization reaction. Pure. Appl. Chem. 1989; 61: 1747-1754.

34. Inderwildi, O.R., Jenkins, S.J., King, D.A, Fischer−Tropsch mechanism revisited: Alternative pathways for the production of higher hydrocarbons from synthesis gas., J. Phys. Chem. C., 2008; 112: 1305-1307.

35. Ojeda, M., Iglesias, E., Nabar, R., Nilekar, A., Mavrikakis, A. Fischer-Tropsch synthesis catalysis: Low temperature Fe catalysts and the mechanism for CO dissociation on Fe and CO., Presented at the 20th NAM, Houston, TX., USA 2007; 17-22.

36. Ojeda, M., Li, A., Nabar, R., Nilekar, A.U., Mavrikakis, M., Iglesias, E., Kinetically relevant steps and H_2/D_2 isotope effects in Fischer−Tropsch synthesis on Fe and Co catalysts., J. Phys. Chem. C. 2010; 114: 19761-19770.

37. Ojeda, M., Nabar, R., Nilekar, A. U., Ishikawa, A., Mavrikakis, M., Iglesia, E., CO activation pathways and the mechanism of Fischer–Tropsch synthesis., J. Catal. 2010; 272: 287-297.

38. Govender, N.S., Botes, F. G., de Croon, M. H. J. M, Schouten, J. C. Mechanistic pathway for methane formation over an iron-based catalyst., J. Catal. 2008; 260: 254-261.

39. Yang, J., Qi, Y., Zhu, J., Zhu, Y., Chen, D., Holmen, A., Reaction mechanism of CO activation and methane formation on Co Fischer–Tropsch catalyst: A combined DFT, transient, and steady-state kinetic modeling., J. Catal. 2013; 308: 37-49.

40. Bian, Z., Miao, X., Lei, S., Chen, S., Wang, W., Struthers, S., The challenges of reusing mining and mineral-processing wastes., Science 2012; 337: 702-703.

41. Balakrishnan, M., Batra, V.S., Hargreaves, J.S.J., Pulford, I.D., Waste materials-catalytic opportunities: An overview of the application of large-scale waste materials as resources for catalytic applications., Green Chem. 2011; 13: 16-24.

42. Khan, A.M., Fatima, N., Hussain, M.S., Yasmeen, K. Biodiesel production from green seaweed Ulva fasciata catalyzed by novel waste catalysts from Pakistan Steel Industry., Chin. J. Chem. Eng. 2016; 24: 1080-1086.

43. Das, B., Prakash, S., Reddy, P.S.R., Misra, V.N., An overview of utilization of slag and sludge from steel industries., Resour. Conserv. Recycl. 2007; 50: 40-57.

44. Drobíková, K., Vallová, S., Motyka, O., Mamulová Kutláková, K., Plachá, D., Seidlerová, J., Effects of binder choice in converter and blast furnace sludge briquette preparation: Environmental and practical implications., Waste Management 2018; 79: 30-37.

45. Frey, A., Goeke, V., Voss, C., Steel gases as ancient and modern challenging resource; historical review, description of the present, and daring vision., Chemie Ingenieur Technik 2018; 90: 1384-1391.

46. Stiessel, S., Berger, A., Fernández, E., Ziegmann, M., Methodology for the evaluation of CO_2-based syntheses by coupling steel industry with chemical industry., Chemie Ingenieur Technik, 2018; 90: 1392-1408.

47. Omran, M., Fabritius, T., Improved removal of zinc from blast furnace sludge by particle size separation and microwave heating., Minerals Engineering 2018; 127:265-276.

48. Mombelli, D., Mapelli, C., Barella, S., Gruttadauria, A., Spada, E., Jarosite wastes reduction through blast furnace sludges for cast iron production., J. Env. Chem. Eng. 2019; 7: 102966.

49. Hussain,I.,Jalil, A.A., Mamat, C.R., Siang, T.J., Rahman, A.F.A., Azami, M.S., Adnan, R.H., New insights on the effect of the H_2/CO ratio for enhancement of CO methanation over metal-free fribrous silica ZSM-5. Thermodynamic and mechanistic studies, Energy Conversion and Management 2019; 199: 112056.

50. Weisz P.B., Prater, C. D., Interpretation of measurements in experimental catalysis. Adv. Catal. 1954; 6: 143-196.

51. Oliveira, L.C.A., Fabris, J.D., Rios, R.R.V.A., Mussel, W.N., Lago, R.M., Fe_3x $MnxO_4$ catalysts: Phase transformations and carbon monoxide oxidation., Appl. Catal. A: General 2004; 259: 253–259.

52. Jozwiak, W.K., Kaczmarek, E., Maniecki, T.P., Ignaczak, W., Maniukiewicz, W., Reduction behavior of iron oxides in hydrogen and carbon monoxide atmospheres.,Appl. Catal. A: General 2007; 326: 17–27.

53. Vereš, J., Lovás, M., Jakabský, Š., Šepelák, V., Hredzák, S., Characterization of blast furnace sludge and removal of zinc by microwave assisted extraction., Hydrometallurgy 2012; 129-130: 67-73.

54. Mikhailov, I., Komarov. S., Levina, V., Gusev, A., Issi, J., Kuznetsov, D., Nanosized zero-valent iron as Fenton-like reagent for ultrasonic-assisted leaching of zinc from blast furnace sludge., J. Hazard. Mater. 2017; 321: 557-565.

55. Steer, J.M., Griffiths, A.J., Investigation of carboxylic acids and non-aqueous solvents for the selective leaching of zinc from blast furnace dust slurry., Hydrometallurgy 2013; 140: 34-41.

56. Amorim, C.C., Dutra P.R., Leão, M.M.D., Pereira, M.C., Henriques, A.B., Fabris, J.D., Lago, R.M., Controlled reduction of steel waste to produce active iron phases for environmental applications., Chem. Eng. J. 2012; 209: 645-651.

57. Wenguang Du, Song Yang, Feng Pan, Ju Shangguan , Jie Lu, Shoujun Liu, and Huiling Fan, Hydrogen Reduction of Hematite Ore Fines to Magnetite Ore Fines at Low Temperatures, Hindawi Journal of Chemistry 2017; Article ID 1919720, https://doi.org/10.1155/2017/1919720

58. Gao, Z., Liao-sha, L., Zhao-jin, W., Xing-mei, S., Hui-hong, L., Shi-huai, S., Effects of microwave heating on pore fractal properties of blast furnace sludge., J. Iron Steel Res. Int. 2013; 20: 27-33.

59. Van Santen, R.A., Complementary Structure Sensitive and Insensitive Catalytic Relationships, Acc. Chem. Res. 2009; 42: 57-66.

60. Das, C.K., Das, N.S., Choudhury, D.P., Ravichadran, G., Chakrabarty, D.K., Hydrogenation of carbon monoxide on unsupported Fe-Mn-K catalyst for the synthesis of lower alkenes: promoter effect of manganese., Appl. Catal. A: General 1994; 111: 119-132.

61. Nakhaei P. A., et al., Effect of Mg, La and Ca promoters on the structure and catalytic behavior of iron-based catalysts in Fischer-Tropsch synthesis., Appl. Catal. A. General 2008; 382(2): 201-208.

62. Li, S., Li, A., Krishnamoorthy, S., Iglesia, E., Effects of Zn, Cu and K Promoters on the structure and on the reduction, carburization, and catalytic behaviour of iron-based Fischer-Tropsch synthesis catalysts., Catal. Lett. 2001; 77(4): 197-205.

63. Wan, H., Wu, B., Tao, Z., Li, T., An, X., Xiang, H., Li, Y., Study of an iron-based Fischer-Tropsch synthesis catalyst incorporated with SiO_2., J. Mol. Catal. A-Chem. 2006; 260(1-2): 255-263.

64. Yang, J., Sun, Y., Tang, Y., Liu, Y., Wang, H., Tian, L., Wang, H., Zhang, Z., Xiang, H., Li, Y., Effect of magnesium promoter on iron-based catalyst for Fischer-Tropsch synthesis., J. Mol. Catal. A-Chem. 2006; 245 (1-2): 26-36.

65. Sehested, J., Dhal, S., Jacobsen, J., Rostrup-Nielsen, J.R., Methanation of CO over nickel: Mechanism and kinetics at High H_2/CO Ratios., J. Phys. Chem. B. 2005; 109: 2432-2438.

66. Escobar, M., Gracia, F., Karelovic, A., Jiménez, R., Kinetic and in situ FTIR study of CO methanation on a Rh/Al_2O_3 catalyst., Catal. Sci. Technol. 2015; 5: 4532-4541.

67. Barrientos, J., Montes, V., Boutonnet, M., Järás, S., Further insights into the effect of sulfur on the activity and selectivity of cobalt-based Fisher-Tropsch catalysts, Catal. Today 2016; 275:119-126.

68. Ma, W., Jacobs, G., Sparks, D.E., Todic, B., Bukur, D.B., Quantitative comparison of iron and cobalt based catalysts for the Fisher-Tropsch synthesis under clean and poisoning conditions, Catal. Today 2020; 343: 125-136.

69. Bartholomew, C.H., Mechanisms of Nickel Catalyst Poisoning, in Studies in Surface Science and Catalysis, B. Delmon and G.F. Froment Editors. 1987, Elsevier. p. 81-104.

70. Yue Yu, Guo-Qiang Jin, Ying-Yong Wang, Xiang-Yun Guo, Synthetic natural gas from CO hydrogenation over silicon carbide supported nickel catalysts, Fuel Processing Technol. 2011; 92 (2), 2293-2298.

71. Dalla Betta, R.A., Piken, A.G., Shelef, M., Heterogeneous methanation: Steady state rate of CO hydrogenation on supported ruthenium, nickel and rhenium, J. of Catalysis 1975; 40,173-183.

SUPPLEMENTARY INFORMATION

Mass and energy criteria for kinetic limitations

Mears criteria for external diffusion limitations [1]:

$$C_{M-D} = \frac{-r'_{CO} \cdot R_p \cdot n}{C_0 \cdot k_m} \ll 0.15 \qquad (1)$$

C_{M-D}= Mears coefficient for external diffusion limitations

$-r'_{CO}$= Observed reaction rate per unit particle volume [mol/cm$^{3\cdot}$s]

R_p= Radius of the particle [cm]

n = Reaction order

C_0= Reactant concentration [mol/cm^3]

k_m= Mass transfer coefficient [cm/s]

The study case is the feed condition 100 ml/min of CO:H_2:N_2=1:20:79 at 350ºC.

$-r'_{CO}$ $\left[\frac{mol}{cm^3 s}\right]$	R_p [cm]	C_0 $\left[\frac{mol}{cm^3}\right]$	n^*
8.98E-08	6.35E-03	1.93E-07	0.5

**Considering the apparent order of the reaction as a function of CO partial pressure.*

The expression of Thoenes and Kramers was used to obtain k_m [2]:

$$k_m = \left(\frac{D_b^4 \cdot (1-\varepsilon)^3 \cdot V^3 \cdot \rho}{d_p^3 \cdot \varepsilon^6 \cdot \mu}\right)^{\frac{1}{6}} \quad (2)$$

D_b= Reactive diffusivity [cm^2/s]

ε= Porosity of the catalytic bed

V= Transversal rate through the reactor [cm/s]

ρ= Gas feed density [g/cm^3]

d_p= diameter of the BFS pellet [cm]

μ= Dynamic viscosity [g/cm·s]

$D_b \left[\frac{cm^2}{s}\right]$	ε	$V \left[\frac{cm}{s}\right]$	$\rho \left[\frac{g}{cm^3}\right]$	$d_p[cm]$	$\mu \left[\frac{g}{cm \cdot s}\right]$
29.2	0.36	8.40	4.46-04	0.0127	2.95E-04

Replacing in (2):

$$k_m = 579.9\ cm/s$$

Finally, from (1):

$$C_{M-D} = 2.55E-06$$

As C_{W-D} is significantly lower than 0.15, internal diffusion limitations are negligible.

<u>Weisz-Prater criteria for internal diffusion limitations [3]:</u>

$$C_{W-P} = \frac{-r'_{CO} \cdot R_p^2}{C_s \cdot D_{eff}} \ll 0.3 \qquad (3)$$

C_{W-P}= Weisz-Prater coefficient

$-r'_{CO}$= Observed reaction rate per unit particle volume [mol/cm$^{3\cdot}$s]

R_p= Radius of the particle [cm]

C_s= Reactant concentration at external surface of the particle [mol/cm^3]

D_{eff}= Effective diffusivity [cm^2/s]

The study case is the feed condition 100 ml/min of CO:H_2:N_2=1:20:79 at 350ºC.

$-r'_{CO}$ $\left[\frac{mol}{cm^3 s}\right]$	R_p [cm]	C_s $\left[\frac{mol}{cm^3}\right]$	D_{eff} $\left[\frac{cm^2}{s}\right]$
8.98E-08	6.35E-03	1.93E-07	0.464

Replacing the parameters on expression (3):

$$C_{W-P} = 4.05E - 05$$

As C_{W-P} is significantly lower than 0.3, internal diffusion limitations are negligible.

<u>Mears criteria for external thermal limitations [4]:</u>

$$C_{M-T} = \left| \frac{-\Delta H_{rx} \cdot R_p \cdot (-r'_{CO}) \cdot E_{ap}}{h \cdot T^2 \cdot R} \right| \ll 0.15 \qquad (4)$$

C_{M-T}= Mears coefficient for thermic limitations

$-\Delta H_{rx}$ = Heat of chemical reaction [J/mol]

R_p= Radius of the particle [m]

$-r'_{CO}$= Observed reaction rate per unit particle volume [mol/m^3·s]

E_{ap}= Activation energy for catalytic reaction [J/mol]

h = Gas-solid heat transfer coefficient

T = Absolute temperature [K]

R = Gas constant [J/mol·K]

$-\Delta H_{rx}$ [J/mol]	R_p [m]	$-r'_{CO}$ $\left[\frac{mol}{s \cdot m^3}\right]$	E_{ap} $\left[\frac{J}{mol}\right]$	T [K]
2.06E+05	6.35E-05	8.98E-02	93.2E+05	623.15

Using Thoenes and Kramers expression [2],

$$h = \frac{k}{\varepsilon}\left(\frac{V \cdot (1-\varepsilon)^3}{d_p \cdot \alpha}\right)^{0.5} \cdot Pr^{1/3} \quad (5)$$

k= Thermal conductivity [W/m·K

ε= Porosity of the catalytic bed

V= Transversal rate through the reactor [m/s]

d_p= diameter of the BFS pellet [m]

α = cinematic viscosity [m^2/s]

Pr= Prandtl number (0.667)

k [W/mK]	ε	$V\ [m/s]$	$d_p[m]$	$\alpha\ [m^2/s]$
75	0.36	8.40E-02	1.27E-04	6.62E-05

Replacing in (5):

$$h = 2.95E + 05\ \left[\frac{W}{m \cdot K}\right]$$

Finally, from (4):

$$C_{M-T} = 1.15E - 07$$

As C_{M-T} is significantly lower than 0.15, thermal limitations are negligible.

References

[1] Fogler, H.; "*Element of chemical reaction engineering, 4º edition*" Prentice Hall, 1986.

[2] D. Thoenes, Jr. and H. Kramers, Chem. Eng. Sci., 8, 271 (1958)

[3] Weisz, P., Prater, C.; "*Interpretation of measurements in experimental catalysis*", Advances in Catalysis, 1954, Vol. 6, p. 143-196.

[4] Mears, D.E., Diagnostic criteria for heat transport limitations in fixed bed reactors. Journal of Catalysis, 1971. 20(2): p. 127-131.

Thermodynamic Calculations

Thermodynamic equilibrium was calculated for the experimental conditions used in this work for the kinetic assays. Aspen plus was used (Gibbs reactor)

Results show complete conversion for CO.

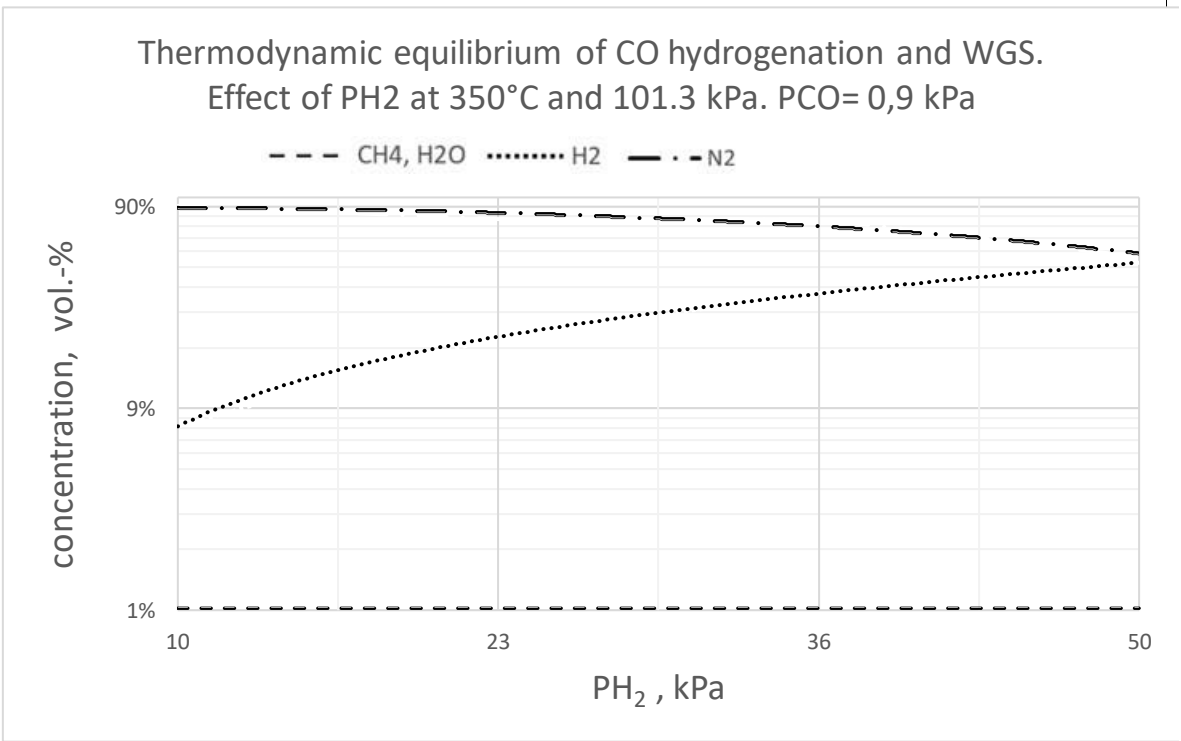

PH2 : 10 - 50 kPa ; PCO= 0.9 kPa (const.)			
"11/1"	"26/1"	"40/1"	"56/1"

P_tot	101,32	P_tot	101,32	P_tot	101,32	P_tot	101,32
P_H2	**10**	P_H2	**23**	P_H2	**36**	P_H2	**50**
P_CO	0,9	P_CO	0,9	P_CO	0,9	P_CO	0,9
P_N2	90,42	P_N2	77,42	P_N2	64,42	P_N2	50,42
%_H2	0,099	%_H2	0,227	%_H2	0,355	%_H2	0,493
%_CO	0,009	%_CO	0,009	%_CO	0,009	%_CO	0,009
%_N2	0,892	%_N2	0,764	%_N2	0,636	%_N2	0,498
H2/CO	11	H2/CO	26	H2/CO	40	H2/CO	56

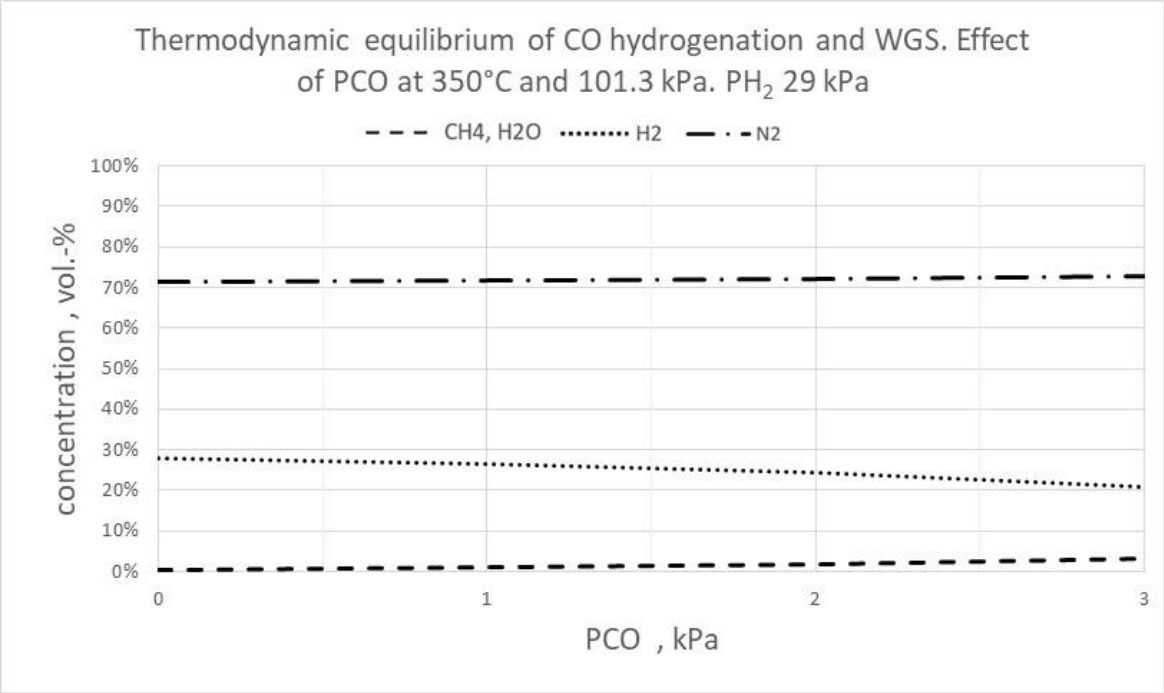

PCO: 0.25 - 3 kPa ; PH2 =29 kPa (const.)							
	"116/1"		"30/1"		"18/1"		"10/1"
P_tot	101,32	P_tot	101,32	P_tot	101,32	P_tot	101,32
P_H2	29	P_H2	29	P_H2	29	P_H2	29
P_CO	**0,25**	P_CO	**0,95**	P_CO	**1,65**	P_CO	**3**
P_N2	72,07	P_N2	71,37	P_N2	70,67	P_N2	69,32
%_H2	0,286	%_H2	0,286	%_H2	0,2862	%_H2	0,286
%_CO	0,002	%_CO	0,009	%_CO	0,0163	%_CO	0,030
%_N2	0,711	%_N2	0,704	%_N2	0,6975	%_N2	0,684
H2/CO	116	H2/CO	31	H2/CO	18	H2/CO	10

Approach to Equilibrium

The following reactions where considered to determinate the equilibrium conditions in this study:

$$CO + 3H_2 \leftrightarrow CH_4 + H_2O \qquad (CO\ methanation)$$
$$CO + H_2 \leftrightarrow CO_2 + H_2O \qquad (WGS)$$

The approach to equilibrium (η) leads to quantify the thermodynamic equilibrium effect on the kinetics rates measured and correct them to obtain forward reaction rates. For the

reaction studied in this work (CO methanation and WGS), η is defined as the ratio between the products and reactants divided by the equilibrium constant, that is [1]:

$$\eta_{MET} = \frac{1}{K_{eq\ CH_4}}\left(\frac{P_{CH_4}P_{H_2O}}{P_{CO_2}P_{H_2}^3}\right) \quad \text{(ec. 1)}$$

$$\eta_{WGS} = \frac{1}{K_{eq\ WGS}}\left(\frac{P_{CO_2}P_{H_2O}}{P_{CO}P_{H_2}}\right) \quad \text{(ec. 2)}$$

Equilibrium constants are given in the following table:

T [ºC]	Keq CH_4	Keq WGS
320	3.22.E+06	31.34
350	1.84.E+09	21.33

Replacing the data in the expressions ec.1 and ec.2 it is possible to conclude that the conditions explored in this work are far from the equilibrium.

	P_{H2} [kPa]	P_{CO} [kPa]	QMET	QWGS	η_{MET}	η_{WGS}
350ºC	38.60	0.91	9.88.E-04	2.02	2.53E-09	9.48.E-02
	14.39	0.91	3.29.E-03	1.39	8.40E-09	6.49.E-02
	28.52	1.32	1.10.E-03	1.53	2.81E-09	7.15.E-02
	29.99	0.49	1.89.E-03	2.79	4.82E-09	1.31.E-01
	27.51	2.35	1.22.E-03	0.86	3.11E-09	4.04.E-02
	29.28	0.93	1.16.E-03	1.99	2.96E-09	9.34.E-02

	27.97	2.02	1.15.E-03	1.01	2.93E-09	4.74.E-02
	49.73	0.95	7.75.E-04	1.82	1.98E-09	8.52.E-02
	29.54	1.79	9.21.E-04	1.18	2.35E-09	5.53.E-02
	19.35	0.92	1.76.E-03	2.02	4.50E-09	9.45.E-02
	28.52	0.89	3.42.E-04	3.61	1.06E-10	1.15.E-01
	29.21	1.73	3.10.E-04	2.00	9.64E-11	6.37.E-02
	29.13	0.46	4.66.E-04	4.35	1.45E-10	1.39.E-01
	24.06	0.90	3.92.E-04	3.27	1.22E-10	1.04.E-01
320ºC	39.58	0.92	1.66.E-04	4.09	5.17E-11	1.31.E-01

CO conversions during Kinetic Assays

The CO conversions obtained during the catalytic assay for a total flow of 100 ml/min are presented in the following table.

Temperature	Condition	Theoretical feed ratio	CO conversion
350 °C	1	1%CO 40%H_2	4.5%
	2	1%CO 15%H_2	2.9%
	3	1,5%CO 30%H_2	2.7%
	4	0,5%CO 30%H_2	6.2%
	5	3%CO 30%H_2	2.0%
	6	1%CO 30%H_2	3.5%
	7	2.5%CO 30%H_2	2.2%

	8	1%CO 50%H_2	5.7%
	9	2%CO 30%H_2	2.4%
	10	1%CO 20%H_2	2.6%
320°C	1	1%CO 30%H_2	2.1%
	2	2%CO 30%H_2	1.5%
	3	0,5%CO 30%H_2	4.1%
	4	1%CO 25%H_2	1.9%
	5	1%CO 40%H_2	2.2%